

# Evaluation of Efficiency and Power Factor in 3-kW GaN-Based CCM/CRM Totem-Pole PFC Converters for Data Center Application

Chen Song, Hui Li  
University of Electronic Science and Technology of China, China

**Abstract**—GaN-based totem-pole power factor correction (PFC) is widely used for data center applications to achieve high efficiency and high power density. In this paper, a design of GaN-based continuous conduction mode (CCM) and critical conduction mode (CRM) totem-pole PFC converters is proposed. Based on simulation and experiment, the efficiency and power factor (PF) for 3-kW applications in CCM and CRM are evaluated. It is concluded that, at the same 3-KW power level, although the CCM operation has lower peak current, the CRM operation shows a higher efficiency with smaller inductor size and moderate PF, thus more promising for the data center applications.

**Index Terms**—GaN devices, totem-pole PFC, CCM, CRM

## I. INTRODUCTION

For the data center application, high efficiency and power factor (PF) AC/DC converters are required [1]. For the 80 Plus Titanium certification in Table I, the efficiency should be more than 90% and the PF should exceed 0.95 even at 20% load conditions. The massive use of nonlinear load equipment in data centers causes the harmonic currents in the supply, which seriously affects the safety and stability of the data center supply system. In order to improve the efficiency and solve the problem of harmonic power supply in data centers, a power factor correction (PFC) is required.

TABLE I. 80 plus certification at 115V

Load	80 Plus	80 Plus Gold	80 Plus Titanium
20%	80%	82%	90% / PF 0.95
50%	80%	85% / PF 0.9	94%
100%	80% / PF 0.9	82%	90%

Recently, the traditional topology has been replaced by the totem-pole PFC for its high efficiency, simple topology, low conduction loss, and high utilization of devices and components [2]. However, for the high-power applications, the Si-based totem-pole PFC topology is not suitable for the continuous conduction mode (CCM) operation. Attributed to the small body diode reverse-recovery effect of the GaN devices, the GaN-based totem-pole PFC topology become a popular solution [3]. Although the GaN-based CCM PFC converters can achieve a high PF, they are inherently limited by the switching losses, which can be addressed by the use of critical conduction mode (CRM).

Lots of early works have been conducted on the CCM/CRM operations. In [4], [5] the zero voltage switching (ZVS) or

valley switching can be achieved in the CRM to reduce the switching loss for higher efficiency. However, CRM operates under the varying frequency range and thus higher current ripple [6]. In the light load condition, it is hard to achieve a high-power quality over the entire load conditions for PFC converters [7]. In [8], a comparison of CCM- and CRM-based active power decoupler was made, but there is little comparison about the GaN-based converters. Moreover, the different load conditions and switching frequency can affect the efficiency and PF, which complicates the design of PFC converters. Therefore, it is necessary to evaluate the efficiency and PF of GaN-based PFC in CCM and CRM.

In this paper, a design of 3-kW GaN-based CCM/CRM totem-pole bridgeless PFC converters is proposed in Section 2. The efficiency and PF are evaluated in Section 3. Conclusions are summarized in Section 4.

## II. DESIGN OF CCM- AND CRM-BASED PFC CONVERTERS

The topology of GaN-based totem-pole PFC is shown in Fig. 1. The GaN devices  $S_1$ ,  $S_2$  operate at the high frequency, and  $S_3$ ,  $S_4$  work at the AC line frequency. During the positive half line cycle,  $S_4$  is always on,  $S_3$  is always off,  $S_2$  is the active switch, and  $S_1$  is the synchronous switch. During the negative half line cycle,  $S_3$  is always on,  $S_4$  is always off,  $S_1$  is the active switch, and  $S_2$  is the synchronous switch.

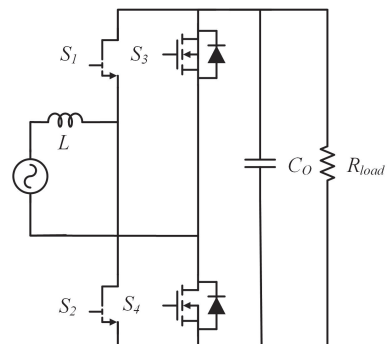


Fig. 1. Topology of totem-pole PFC

### A. The operation principle of CCM- and CRM-based PFC

Fig. 2 shows the operation progress stages for CCM totem-pole PFC. During stage 1,  $S_2$  is on and  $S_1$  is off, causing  $L$  to

store energy and its current rises linearly. During stage 2,  $S_1$  turns on and  $S_2$  is off, causing the inductor current decreases linearly. At the negative half cycle,  $S_1$  is on and  $S_2$  is off at stage 3, the inductor current rises linearly.  $S_2$  is on and  $S_1$  is off at stage 4, the inductor current decreases linearly.

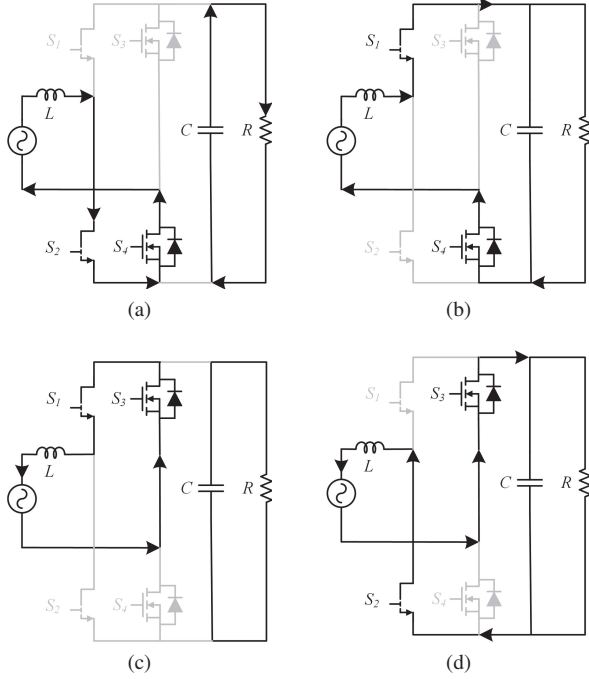


Fig. 2. Operation process stages of CCM totem-pole PFC, (a) Stage 1, (b) Stage 2, (c) Stage 3, (d) Stage 4.

Fig. 3 shows the operation progress stages for CRM totem-pole PFC based on the positive cycle. Each switching cycle can be separated into six stages. During stage 1,  $S_2$  is on and  $S_1$  is off, the inductor current rises linearly. During stage 2,  $S_1$  and  $S_2$  is off, the inductor current resonate with the junction capacitors of two MOSFET. During stage 3,  $S_1$  is on and  $S_2$  is off, the inductor current decreases linearly. During stage 4, the inductor current continues to decrease and becomes negative current. During stage 5, it turns to the resonance stage like the stage 2. During stage 6,  $S_1$  is off and  $S_2$  is on, the negative current rises linearly.

#### B. The control design for CCM- and CRM-based PFC

The totem-pole PFC converter control system is a dual closed-loop voltage and current control system. Fig. 4(a) and (b) illustrate the control loop diagrams for CCM and CRM, respectively. For CCM, the average current method is used to achieve high gain bandwidth and high PF. Using the product of the voltage loop output and the grid voltage as the reference value of the inductor current, the grid voltage and the inductor current has the same phase, and the waveform is sinusoidal.

Before designing the control system, the converter needs to be modeled. The state-space average method is used to derive the power stage transfer function. According to the state of GaN devices, the equivalent circuit diagram for a single switching cycle is shown in Fig. 5(a) and (b). The on and off

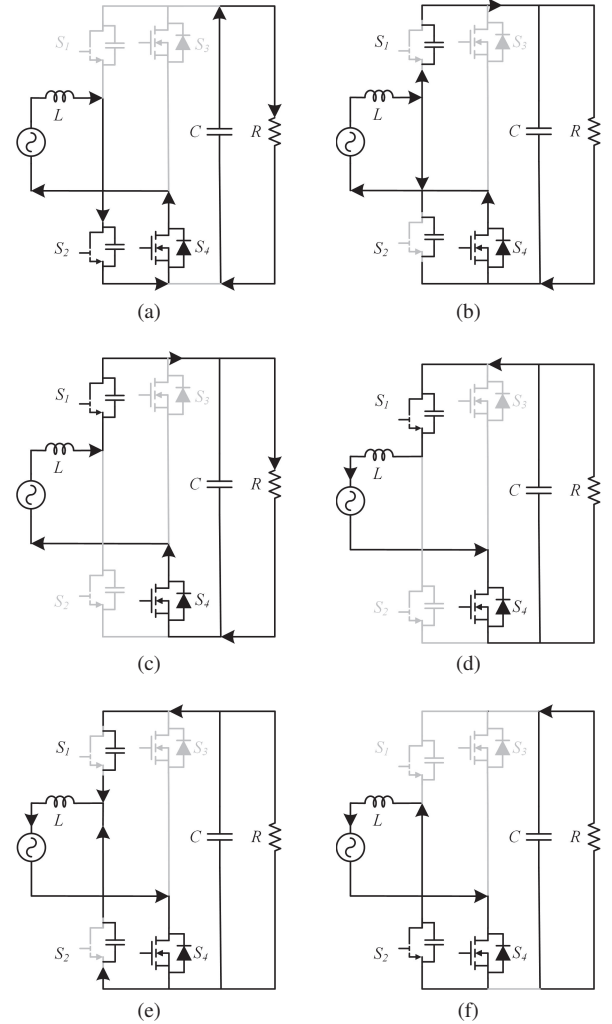


Fig. 3. Operation process stages of CRM totem-pole PFC, (a) Stage 1, (b) Stage 2, (c) Stage 3, (d) Stage 4, (e) Stage 5, (6) Stage 6.

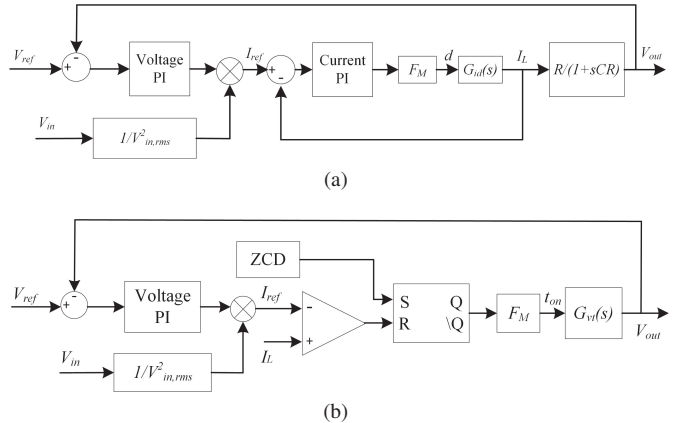


Fig. 4. Control loop of totem-pole PFC, (a) CCM, (b) CRM.

states are depicted in (1)(2), where  $I_L$  is the inductor current and  $V_O$  is the output voltage.

$$\begin{bmatrix} i_L(t) \\ V_O(t) \end{bmatrix} = \begin{pmatrix} 0 & 0 \\ 0 & -\frac{1}{RC} \end{pmatrix} \begin{pmatrix} i_L(t) \\ V_O(t) \end{pmatrix} + \begin{pmatrix} \frac{1}{L} \\ 0 \end{pmatrix} (V_{in}(t)) \quad (1)$$

$$\begin{bmatrix} i_L(t) \\ V_O(t) \end{bmatrix} = \begin{pmatrix} 0 & -\frac{1}{L} \\ \frac{1}{C} & -\frac{1}{RC} \end{pmatrix} \begin{pmatrix} i_L(t) \\ V_O(t) \end{pmatrix} + \begin{pmatrix} \frac{1}{L} \\ 0 \end{pmatrix} (V_{in}(t)) \quad (2)$$

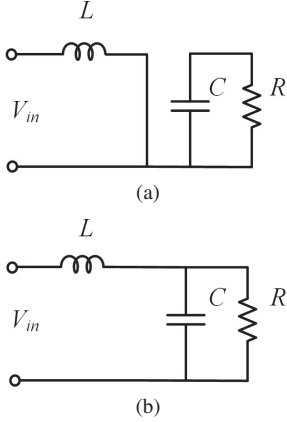


Fig. 5. Totem-pole PFC circuit single switching cycle equivalent circuit diagram, (a) On, (b) Off.

Using  $d$  for duty cycle, the matrix  $A$  is defined as (3), and  $B$  is defined as (4), the small-signal state-space average equation is shown in (5).

$$A = \begin{pmatrix} 0 & 0 \\ 0 & -\frac{1}{RC} \end{pmatrix} d + \begin{pmatrix} \frac{1}{L} \\ 0 \end{pmatrix} (1-d), A = A_1 d + A_2 (1-d) \quad (3)$$

$$B = \begin{pmatrix} 0 & -\frac{1}{L} \\ \frac{1}{C} & -\frac{1}{RC} \end{pmatrix} d + \begin{pmatrix} \frac{1}{L} \\ 0 \end{pmatrix} (1-d), B = B_1 d + B_2 (1-d) \quad (4)$$

$$\hat{x} = A\hat{x} + B\hat{u} + [(A_1 - A_2)X + (B_1 - B_2)U]\hat{d} \quad (5)$$

Where  $X$  is the state vector  $[I_L V_O]^T$ ,  $U$  is the input vector  $V_{in}(t)$ ,  $D$  is the duty. After the Laplace transform, the power stage transfer function can be obtained, and the simplified duty-to-output-current transfer function is derived in (6). The loop gain of the current control in CCM operation is

$$G_{id} = \left. \frac{i_d}{d} \right|_{V_{in}=0} = \frac{(1-D)I_L + (sC + \frac{1}{R})V_O}{LCs^2 + \frac{L}{R}s + (1-D)^2} \approx \frac{V_O}{Ls} \quad (6)$$

$$T_{i,CCM} = G_{ic}G_{id} \quad (7)$$

In this section, the  $f_{sw} = 65\text{kHz}$ , and the  $G_{ic}$  is the gain of PI controller in current loop, and the PI compensator is designed to have 3 kHz control bandwidth.

Output current can be derived by (8). Where  $P_O$  is the output power. Assuming that the output power is equal to the input power, the reference current can be denoted as (9). According to Fig. 4(a), the reference current can also be denoted by the output of voltage loop shown in (9).

$$i_O = C \frac{dV_O}{dt} + \frac{P_O}{V_O} \quad (8)$$

$$I_{ref} = \frac{\sqrt{2}P_{in}}{V_{rms}} \sin(wt) = \frac{\sqrt{2}V_{vo}}{V_{rms}} \sin(wt) \quad (9)$$

$$\hat{i}_O = C \frac{d\hat{V}_O}{dt} - \frac{I_O}{V_O} \hat{V}_O \quad (10)$$

$$\hat{i}_O = \frac{\hat{V}_{VO}}{V_O} - \frac{i_O}{V_O} \hat{V}_O \quad (11)$$

Implementing perturbation and linearization on (8) and (9), the small-signal result is (10) and (11). Combining (10) and (11), the transfer function and the loop gain of voltage can be derived:

$$G_{vv} = \frac{1}{sCV_O} \quad (12)$$

$$T_{v,CCM} = G_{vc}G_{vv} \quad (13)$$

$G_{vc}$  is the gain of PI controller in voltage loop, the PI compensator is designed to have 3 Hz control bandwidth.

For CRM operation, the variable on-time control is used to achieve high PF and control the current within reference current  $I_{ref}$ . If the inductor current is approaching zero, ZCD signal would enable the SR register and open the active switching device, resulting in variable on-time  $T_{on}$ .

The average inductor current  $I_{L,ave}$  can be simplified as

$$I_{L,ave} \approx \frac{1}{2} \frac{V_{in}}{L} T_{on} \quad (14)$$

$$C \frac{dV_O}{dt} = I_{L,ave} d - \frac{V_O}{R} \quad (15)$$

Using  $d \approx V_{in}/V_{on}$ , the average current can also be denoted as (15). the small-signal result is (16) and (17).

$$\hat{i}_L = \frac{1}{2} \frac{\hat{V}_{in} T_{on} + V_{in} \hat{T}_{on}}{L} \quad (16)$$

$$CV_O \frac{d\hat{V}_O}{dt} = V_{in} \hat{i}_L + \hat{V}_{in} i_L - \frac{V_O \hat{V}_O}{2R} \quad (17)$$

After the Laplace transform, (16) and (17) is in the  $s$  domain, and the on-time-to-output transfer function is derived. As the  $sRC \gg 1$ , to facilitate the calculation, we simplify it as:

$$G_{vt} \approx \frac{V_{in}^2}{2V_O LC s} \quad (18)$$

With 3 kHz control bandwidth for the PI compensator  $G_{tc}$ , the loop gain of it is

$$T_{v,CRM} = G_{tc}G_{vt} \quad (19)$$

### C. The design of power inductor

The minimum value of inductor can be calculated from the (20) and (21). In this work, the values of inductor are  $350 \mu\text{H}$  and  $100 \mu\text{H}$  for CCM and CRM respectively at  $f_{sw,max} = 65 \text{ kHz}$ ,  $P_{out} = 3 \text{ kW}$ ,  $V_{out} = 400 \text{ V}$ . Through AP method, the type of inductor can be determined, as long as (22) is satisfied.

$$L_{CCM} \geq \frac{\sqrt{2}V_{in,RMS}D}{\Delta I_L f_{sw}} \quad (20)$$

$$L_{CRM} \geq \frac{V_{in,RMS}^2}{2P_O}(1 - \frac{\sqrt{2}V_{in,RMS}}{V_O})T_{sw} \quad (21)$$

$$Ap \geq L \frac{I_{in,peak} I_{in,RMS}}{K_U B_{Max} J_{Max}} \quad (22)$$

$J_{Max}$  is the maximum current density,  $B_{Max}$  is the maximum magnetic flux density of the core,  $K_U$  is the window utilization coefficient. Number of turns of the coil is (23).

$$N = \frac{LI_{in,peak}}{A_{e'} B_{Max}} \quad (23)$$

$$\Delta = \frac{75}{\sqrt{f_{sw}}} \quad (24)$$

Where  $A_{e'}$  is the effective core cross-sectional area. The radius of wire should be less than the skin depth  $\Delta$  under  $100^\circ\text{C}$  in (24). The size of the cross-sectional area is

$$S = \frac{I_{in,RMS}}{J_{Max}} \quad (25)$$

The calculation result of inductor parameters is shown in Table II.

TABLE II. Parameters of the inductor

Parameters	CCM	CRM
Core Material	Sendust	Sendust
Type	77716	77083
Size	$51.7 \times 30.9 \times 14.35 \text{ mm}^3$	$39.9 \times 24.1 \times 14.5 \text{ mm}^3$
Air Gap	1.139 mm	1.495 mm
Number of Turns	65	43
Wire Diameter	0.5 mm	0.5 mm

## III. EXPERIMENTAL RESULTS AND DISCUSSION

### A. DPT Experiment

The switching losses of GaN devices are obtained by the double pulse test (DPT) [9], as shown in Fig. 6. The DPT evaluation board consists of DSP, gate driver, GaN half-bridge, current shunt and other parts. Fig. 8 illustrates the typical switching waveforms in the condition of  $V_{DC}=400 \text{ V}$ ,  $i_L=15 \text{ A}$ ,  $R_{on}=10 \Omega$ ,  $R_{off}=4.7 \Omega$ . The turn-on loss  $E_{on}$  and turn-off loss  $E_{off}$  are calculated according to switching waveforms. By this way, the device switching losses can be obtained, which is shown in Fig. 7. The parameters under  $25^\circ\text{C}$  of GaN device is shown in table III

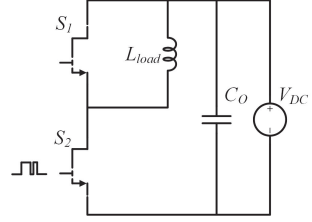


Fig. 6. DPT Topology.

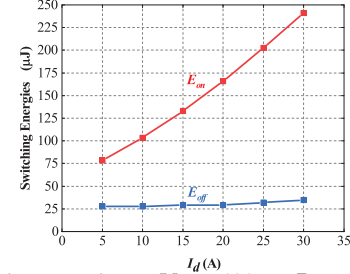


Fig. 7. Switching energies at  $V_{DC}=400 \text{ V}$ ,  $R_{on}=10 \Omega$ ,  $R_{off}=4.7 \Omega$

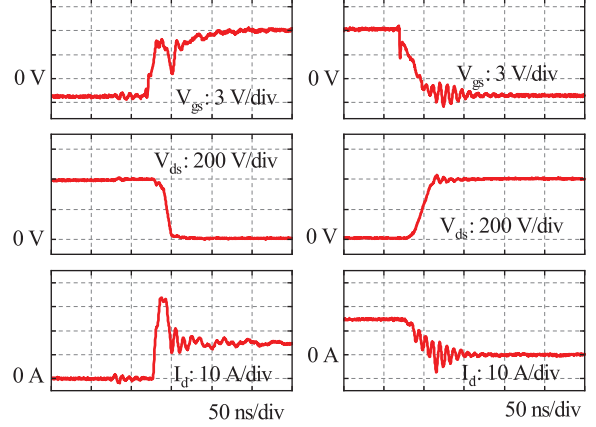


Fig. 8. Switching waveforms at  $V_{DC}=400 \text{ V}$ ,  $i_L=15 \text{ A}$ ,  $R_{on}=10 \Omega$ ,  $R_{off}=4.7 \Omega$ : (a) Turn-on transient, (b) Turn-off transient.

TABLE III. Parameters of GaN devices

Parameters	Value	Unit
Maximum Drain-to-Source Voltage	650	V
Maximum Continuous Drain Current	60	A
On-resistance	25	$m\Omega$
Gate-to-Source Voltage	-10 to 7	V
Reverse Recovery Charge	0	nC

### B. Efficiency

The efficiency of PFC converters is calculated by switching, conduction and inductor losses, while ESR loss is ignored. The turn-on loss  $E_{on}$  and turn-off loss  $E_{off}$  of  $S_1$  and  $S_2$  are obtained by DPT, and switching losses of  $S_3$  and  $S_4$  are ignored. Applying the 2nd-order polynomial fit to  $E_{off}$  -  $I_d$  and  $E_{on}$  -  $I_d$  curve, the switching loss is

$$P_{sw} = f_{sw} \left( \frac{a+i}{2} I_d^2 + \frac{2b+2j}{\pi} I_d + c + k \right) \quad (26)$$

Where  $a$ ,  $b$  and  $c$  is the fitting parameters for  $E_{on}$ , and  $i$ ,  $j$  and  $k$  is the fitting parameters for  $E_{off}$  [10]. Conduction losses, including  $S_1$  to  $S_4$ , are calculated by (27) ( $n = f_{sw}/f_0$ ), and conduction losses during the dead time for  $S_1$  and  $S_2$  are obtained by replacing  $T_{on}$  to  $T_d$ .

$$P_{cond} = \sum_{i=1}^n \int_0^{T_{on}} \left( \frac{I_{L,peak}(i)}{T_{on}} t \right)^2 R_{on} dt = \frac{I_{pk}^2 R_{on} T_{on} f_{sw}}{6\pi f_0} \quad (27)$$

$$P_{cond,deadtime} = \frac{I_{pk}^2 R_{on} T_d f_{sw}}{6\pi f_0} \quad (28)$$

Moreover, inductor losses are determined by parameters in Table II, which consist of copper and iron losses given in (29).

$$P_{Cu} = I_{in,rms}^2 R_{Cu} = 2 I_{in,rms}^2 N \rho \sqrt{\frac{\pi}{S}}, \quad (29)$$

$$P_{Fe} = P_{Fe,unit} V_L = 5.4 \times 10^{-7} \times B^{2.15} f^{1.22} \frac{\mu_0 \mu L I_{in,rms}^2}{B_{max}^2} \quad (30)$$

$$P_{loss} = P_{sw} + P_{cond} + P_{cond,deadtime} + P_{ind} \quad (31)$$

Where  $R_{cu}$  is the resistance value of the copper wire,  $\rho$  is the resistivity of the wire.  $P_{Fe,unit}$  is the unit iron loss of the inductor, which can be obtained by Steinmetz's equation.  $P_{ind}$  is the sum of  $P_{Fe}$  and  $P_{Cu}$ . The total losses of PFC can be denoted as (31).

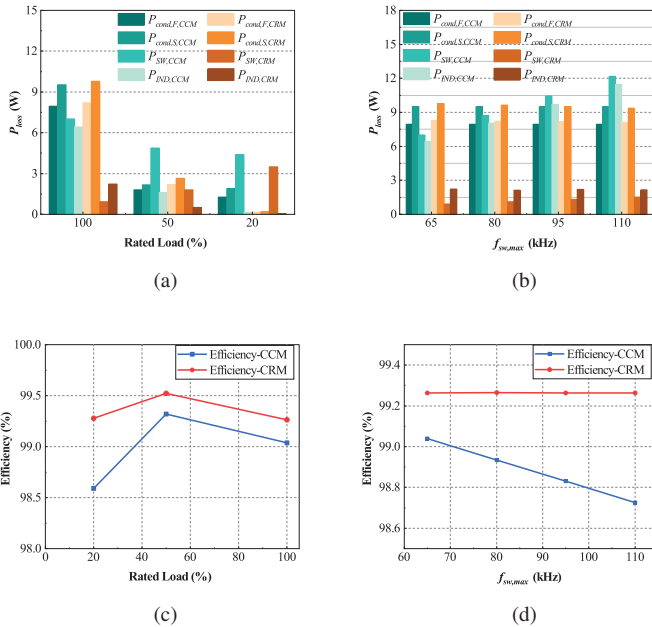


Fig. 9. Power loss and efficiency of CCM- and CRM-based PFC, (a)  $P_{loss}$  at different load, (b)  $P_{loss}$  at different  $f_{sw,max}$ , (c) Efficiency at different load, (d) Efficiency at different  $f_{sw,max}$ .

According to simulation, Fig. 9 illustrates the comparison of efficiency between CCM and CRM with the variations of load condition and  $f_{sw,max}$ . The efficiency of CRM performs much better than CCM, because valley switching can be achieved in CRM to reduce the switching loss. Furthermore, although CRM has higher unit iron loss of inductor, its total inductance

loss is still lower than CCM, owing to its smaller inductor size. As shown in Fig. 9 (a) and (c), the efficiency of half load is higher, due to the decrease in inductor current. In light load conditions, the efficiency decreases because switching loss becomes the dominant. As shown in Fig. 9 (b) and (d), switching losses, drive losses and inductance losses increase with increasing  $f_{sw}$ , leading to the reduction of efficiency in CCM. The inductance decreases with increasing  $f_{sw,max}$ , making just little change in inductance losses of CRM. Above all, without considering the controlling complexity of CRM and its excessive peak current, CRM is better than CCM in terms of efficiency.

### C. Power Factor

Fig. 10 demonstrates the total harmonic distortion (THD) of CCM and CRM at different load conditions. Because of the zero-crossing distortion in totem-pole PFC, circuit contains a relatively large third harmonic. In the rated and half load conditions, the THD of CCM is smaller than CRM, with the PF reaches 99.96%. However, the PF of CCM falls at light load condition, while the PF is unaffected by different load in CRM.

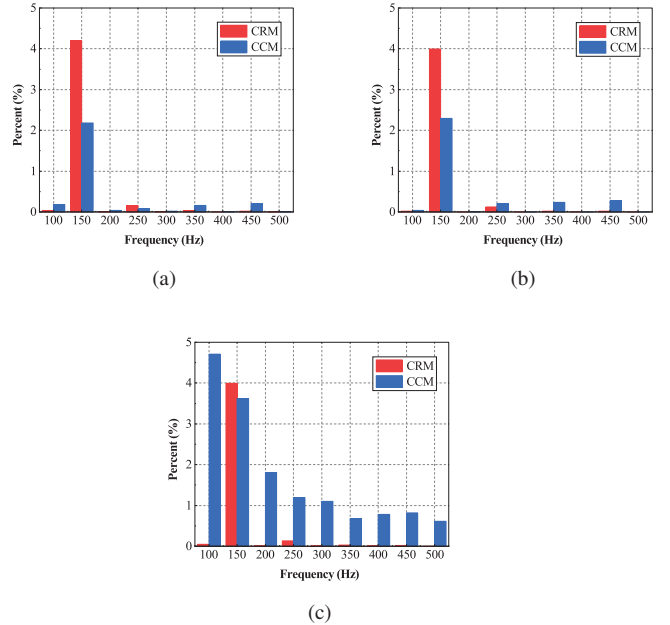


Fig. 10. THD of CCM- and CRM-based PFC at  $f_{sw,max}=65$  kHz,  $L_{CCM}= 350 \mu H$ ,  $L_{CRM}= 100 \mu H$ , (a) Rated Load, (b) 50% rated load, (c) 20% rated load.

Fig. 11 shows the PF at different load conditions and  $f_{sw,max}$ . With CCM operation, changing  $f_{sw}$  has little effect on PF, but it affects  $L_{min}$  and EMC at the design stage. With CRM operation, the same level of PF as CCM can be achieved at  $f_{sw,max}=110$  kHz. The further increase of  $f_{sw,max}$  may lead to a higher PF, but the excessive switching frequency leads to new issues for design stage.

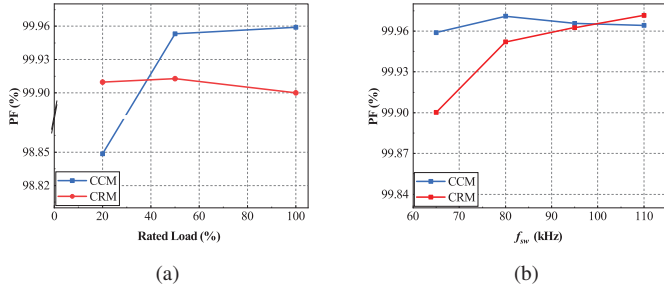


Fig. 11. PF of CCM- and CRM-Based PFC, (a) different load, (b) different  $f_{sw,max}$

#### IV. CONCLUSION

In this paper, a design of 3-kW GaN-based CCM/CRM totem-pole PFC converters is proposed to meet the 80 Plus Titanium certification for data center applications. Based on simulation and experiment results, CRM operation has higher efficiency and its efficiency is independent of frequency, which performs better than CCM operation. From the PF perspective, CCM operation performs slightly better than CRM, and the CRM can show higher PF at the light load condition. To summarize, without considering the difficulties of CRM control, the advantages of smaller inductor and high efficiency make CRM a better choice for 3-kW data center application.

#### REFERENCES

- [1] J. Wu, Y. Qi, F. Muhammad, and X. Wu, "A unified switch loss model and design consideration for multilevel boost pfc with gan devices," *CPSS Transactions on Power Electronics and Applications*, vol. 6, no. 4, pp. 349–358, 2021.

- [2] L. Zhou, Y. Wu, J. Honea, and Z. Wang, "High-efficiency true bridgeless totem pole pfc based on gan hemt: Design challenges and cost-effective solution," in *Proceedings of PCIM Europe 2015; International Exhibition and Conference for Power Electronics, Intelligent Motion, Renewable Energy and Energy Management*, 2015, pp. 1–8.
- [3] Z. Liu, F. C. Lee, Q. Li, and Y. Yang, "Design of gan-based mhz totem-pole pfc rectifier," in *2015 IEEE Energy Conversion Congress and Exposition (ECCE)*, 2015, pp. 682–688.
- [4] J. Sun, J. Li, D. J. Costinett, and L. M. Tolbert, "A gan-based crm totem-pole pfc converter with fast dynamic response and noise immunity for a multi-receiver wpt system," in *2020 IEEE Energy Conversion Congress and Exposition (ECCE)*, 2020, pp. 2555–2562.
- [5] Q. Huang and A. Q. Huang, "Review of gan totem-pole bridgeless pfc," *CPSSTransactions on Power Electronics and Applications*, vol. 2, no. 3, pp. 187–196, 2017.
- [6] N. Korada and R. Ayyanar, "New crm topology for zero voltage switching in quadratic high gain boost converter," in *2020 IEEE Energy Conversion Congress and Exposition (ECCE)*, 2020, pp. 4794–4801.
- [7] H.-S. Youn, J.-B. Lee, J.-I. Baek, J.-W. Kim, C.-O. Yeon, and G.-W. Moon, "A digital leading phase current reduction (lpcr) technique for ccm boost pfc in light load conditions," in *2015 9th International Conference on Power Electronics and ECCE Asia (ICPE-ECCE Asia)*, 2015, pp. 1041–1046.
- [8] Y. Shen, M. D'Antonio, S. Chakraborty, A. Hasnain, and A. Khaligh, "Comparison of ccm- and crm-based boost parallel active power decoupler for pv microinverter," *IEEE Transactions on Power Electronics*, vol. 37, no. 8, pp. 9889–9906, 2022.
- [9] Z. Zhang, B. Guo, F. F. Wang, E. A. Jones, L. M. Tolbert, and B. J. Blalock, "Methodology for wide band-gap device dynamic characterization," *IEEE Transactions on Power Electronics*, vol. 32, no. 12, pp. 9307–9318, 2017.
- [10] S. Yin, Y. Lin, R. Hao, S. Jin, C. He, W. Yao, X. Li, Q. He, X. Pu, X. Su, Y. Zou, H. Cai, K.-J. Lee, M. Wang, H. Guo, K. Shen, F. Wang, H.-C. Chiu, L. Chen, D. Marcon, and R. K.-Y. Wong, "Evaluation of reliability and lifetime of 650-v gan-on-si power devices fabricated on 200-mm cmos-compatible process platform for high-density power converter application," in *2022 IEEE 34th International Symposium on Power Semiconductor Devices and ICs (ISPSD)*, 2022, pp. 93–96.